

Molecular gas in two companion cluster galaxies at $z = 1.2$

G. Castignani^{1,2,*}, F. Combes^{1,2}, P. Salomé¹, S. Andreon³, M. Pannella⁴, I. Heywood^{5,6}, G. Trinchieri³, C. Cicone³,
L. J. M. Davies⁷, F. N. Owen⁸, and A. Raichoor⁹

¹ Sorbonne Université, Observatoire de Paris, Université PSL, CNRS, LERMA, F-75014, Paris, France

² Collège de France, 11 Place Marcelin Berthelot, 75231 Paris, France

³ INAF-Osservatorio Astronomico di Brera, via Brera 28, 20121 Milano, Italy

⁴ Department of Physics, Ludwig-Maximilians-Universität, Scheinerstr. 1, D-81679 München, Germany

⁵ Astrophysics, Department of Physics, University of Oxford, Keble Road, Oxford OX1 3RH, UK

⁶ Department of Physics and Electronics, Rhodes University, PO Box 94, Grahamstown, 6140, South Africa

⁷ International Centre for Radio Astronomy Research, University of Western Australia M468, 35 Stirling Highway, Crawley, WA 6009, Australia

⁸ National Radio Astronomy Observatory, P.O. Box O, Socorro, NM 87801, USA

⁹ Institute of Physics, Laboratory of Astrophysics, Ecole Polytechnique Fédérale de Lausanne (EPFL), Observatoire de Sauverny, 1290 Versoix, Switzerland

Received 23 February 2018 / Accepted 5 June 2018

ABSTRACT

Context. Probing both star formation history and evolution of distant cluster galaxies is essential to evaluate the effect of dense environment on shaping the galaxy properties we observe today.

Aims. We investigate the effect of cluster environment on the processing of the molecular gas in distant cluster galaxies. We study the molecular gas properties of two star-forming galaxies separated by 6 kpc in the projected space and belonging to a galaxy cluster selected from the Irac Shallow Cluster Survey, at a redshift $z = 1.2$, that is, ~ 2 Gyr after the cosmic star formation density peak. This work describes the first CO detection from $1 < z < 1.4$ star-forming cluster galaxies with no clear reported evidence of active galactic nuclei.

Methods. We exploit observations taken with the NOEMA interferometer at ~ 3 mm to detect CO(2-1) line emission from the two selected galaxies, unresolved by our observations.

Results. Based on the CO(2-1) spectrum, we estimate a total molecular gas mass $M(\text{H}_2) = (2.2^{+0.5}_{-0.4}) \times 10^{10} M_\odot$, where fully excited gas is assumed, and a dust mass $M_{\text{dust}} < 4.2 \times 10^8 M_\odot$ for the two blended sources. The two galaxies have similar stellar masses and H α -based star formation rates (SFRs) found in previous work, as well as a large relative velocity of ~ 400 km/s estimated from the CO(2-1) line width. These findings tend to privilege a scenario where both sources contribute to the observed CO(2-1). Using the archival Spitzer MIPS flux at $24 \mu\text{m}$ we estimate an $\text{SFR}(24\mu\text{m}) = (28^{+12}_{-8}) M_\odot/\text{yr}$ for each of the two galaxies. Assuming that the two sources contribute equally to the observed CO(2-1), our analysis yields a depletion timescale of $\tau_{\text{dep}} = (3.9^{+1.4}_{-1.8}) \times 10^8$ yr, and a molecular gas to stellar mass ratio of 0.17 ± 0.13 for each of two sources, separately. We also provide a new, more precise measurement of an unknown weighted mean of the redshifts of the two galaxies, $z = 1.163 \pm 0.001$.

Conclusions. Our results are in overall agreement with those of other distant cluster galaxies and with model predictions for main sequence (MS) field galaxies at similar redshifts. The two target galaxies have molecular gas mass and depletion times that are marginally compatible with, but smaller than those of MS field galaxies, suggesting that the molecular gas has not been sufficiently refueled. We speculate that the cluster environment might have played a role in preventing the refueling via environmental mechanisms such as galaxy harassment, strangulation, ram-pressure, or tidal stripping. Higher-resolution and higher-frequency observations will enable us to spatially resolve the two sources and possibly distinguish between different gas processing mechanisms.

Key words. Galaxies: clusters: individual: ISCS J1426.5+3339; Galaxies: clusters: general; Galaxies: star formation; Molecular data.

1. Introduction

Evolution and growth of galaxies in clusters are believed to be strongly affected by their dense megaparsec-scale environments. In the local Universe, we observe tight correlations between cluster occupancy and galaxy properties such as morphology (Dressler 1980), color (Kodama et al. 2001), stellar mass (Ostriker & Tremaine 1975), active galactic nuclei (AGN) fraction (Kauffmann et al. 2004), star formation (Butcher & Oemler 1984; Peng et al. 2010) and gas content (Gunn & Gott 1972; Chung et al. 2009; Vollmer et al. 2012; Jachym et al. 2014).

There is still debate on the astrophysical processes occurring in clusters which lead to these relations, and the epochs during which they are being established. For example, the cores of nearby rich clusters are largely populated by passive ellipticals, with negligible ongoing star formation (morphology vs. density, and star formation rate vs. density relations, Andreon et al. 2006; Raichoor & Andreon 2012), which to first order is consistent with a burst of star formation at $z \gtrsim 2$, followed by passive evolution to the present day (e.g., Eisenhardt et al. 2008; Mei et al. 2009; Mancone et al. 2010). However, a number of recent studies have found potentially conflicting results to this somewhat simplistic hypothesis, finding a high concentration of potentially in-falling, star-forming galaxies in the outskirts of nearby clusters (e.g., Bai et al. 2009; Chung et al. 2010), and a

* e-mail: gianluca.castignani@obspm.fr

strong evolution of the fraction of star-forming galaxies in cluster cores out to $z \sim 1$ and beyond (Smith et al. 2010; Webb et al. 2013; Brodwin et al. 2013; Zeimann et al. 2013; Alberts et al. 2016). These findings appear to contradict the predictions of early, bursty star formation in cluster core galaxies and suggest the late assembly of cluster members via both strong environmental quenching mechanisms (e.g., strangulation, ram pressure stripping, and galaxy harassment; Larson et al. 1980; Moore et al. 1999) and rapid infall of gas feeding star formation at high- z (reaching a maximum at $z \sim 2$), followed by slow cooling flows at low- z (Salomé et al. 2006, 2008, 2011; Ocvirk et al. 2008; Dekel et al. 2009a,b).

Probing molecular gas in distant clusters is a unique tool to study the star formation history and evolution of cluster galaxies. Advancements of observational facilities at millimeter wavelengths, such as NOEMA and ALMA interferometers, have remarkably increased the statistics of distant $z > 1$ cluster galaxies with detections of molecular gas. Several studies have investigated molecular gas reservoirs of distant $z > 1$ cluster galaxies (see e.g., Noble et al. 2017, and references therein). However, to the best of our knowledge, the cluster galaxy at $z = 1.1147$ of Wagg et al. (2012), classified by the authors as an obscured AGN from the optical spectrum, is the only one in the literature in the redshift range $1 < z < 1.4$ with a reported CO detection.

All remaining studies refer to cluster galaxies in the range $z \sim 1.4 - 2.0$, that is, close to the peak of star formation activity in clusters occurring at $z \sim 2$. We summarize in the following the main results from the literature in this specific redshift range. Aravena et al. (2012) detected CO(1-0) in two galaxies belonging to a cluster candidate at $z \simeq 1.55$. Casasola et al. (2013) detected CO(2-1) in the gas-rich radio galaxy 7C 1756+6520 in cluster environment at $z \simeq 1.4$. Noble et al. (2017) reported the detection of CO(2-1) in 11 gas-rich galaxies belonging to three galaxy clusters at $z \simeq 1.6$. Rudnick et al. (2017) detected CO(1-0) in two galaxies from a confirmed galaxy cluster at $z \simeq 1.6$. Webb et al. (2017) reported the discovery of a large molecular gas reservoir based on CO(2-1) observations of a distant brightest cluster galaxy at $z = 1.7$. Stach et al. (2017) and Hayashi et al. (2017, 2018) detected molecular gas in a sample of 17 galaxies in total, belonging to the cluster XMMXCS J2215.9-1738 at $z \simeq 1.5$. Recently, Coogan et al. (2018) detected molecular gas in a sample of eight cluster galaxies belonging to the distant cluster Cl J1449+0856 at $z = 1.99$.

At even higher redshifts, that is, $z \gtrsim 2$, large reservoirs of molecular gas have commonly been observed in highly star-forming galaxies in proto-clusters, with star formation rates $\text{SFR} \gtrsim 200 M_{\odot}/\text{yr}$ (Papadopoulos et al. 2000; Emonts et al. 2016; Wang et al. 2016; Oteo et al. 2018).

At lower redshifts, $1 < z < 1.4$, the molecular gas content of distant cluster galaxies is still substantially unexplored. Such an epoch is nevertheless important for understanding both the fate of molecular gas in distant cluster galaxies and the mechanisms responsible for the growth of cluster galaxies, as $z \gtrsim 2$ proto-clusters evolve into virialized structures down to $z \sim 0$.

In the present work, we report the detection of CO(2-1) from two unresolved cluster galaxies at $z = 1.2$ obtained with the NOEMA interferometer at the Plateau de Bure. This represents the first CO detection from $1 < z < 1.4$ cluster galaxies with no reported clear evidence of AGNs. Our two selected galaxies are observed significantly later (~ 2 Gyr) than the cosmic star formation density peak occurring at $z \sim 2$ for field galaxies (e.g., Madau & Dickinson 2004), and possibly earlier for (proto-)cluster galaxies (Chiang et al. 2017; Overzier 2016). The two sources have an angular separation of 0.72 arcsec inferred from

their archival Hubble Space Telescope (HST) image (i.e., 6 kpc at the redshift of the sources) and belong to the distant cluster ISCS J1426.5+3339. They are located at an angular separation of ~ 1 arcmin (~ 500 kpc) from the cluster center. The CO detection reported in this work is the first one resulting from a wider search for molecular gas in distant cluster galaxies.

In Sect. 2, we describe the two targets; in Sect. 3 we describe the observations and data reduction; in Sects. 4 and 5 we present and discuss the results, respectively; in Sect. 6 we draw our conclusions.

Throughout this work, we adopt a flat Λ CDM cosmology with matter density $\Omega_m = 0.30$, dark energy density $\Omega_{\Lambda} = 0.70$ and Hubble constant $h = H_0/100 \text{ km s}^{-1} \text{ Mpc}^{-1} = 0.70$ (see however, Planck Collaboration 2016; Riess et al. 2016, 2018). Under these assumptions, the luminosity distance of the target sources is $D_L = 8.024$ Gpc.

2. Two cluster galaxies

We consider the sample of 18 galaxy clusters at $1.0 < z < 1.5$ from the Zeimann et al. (2013) catalog. The clusters belong to the Irac Shallow Cluster Survey (ISCS) that comprises distant clusters detected within the Boötes field of the NOAO Deep Wide-Field Survey (NDWFS; Jannuzi & Dey 1999) using accurate optical/infrared photometric redshifts (Brodwin et al. 2006) and the $4.5 \mu\text{m}$ flux-limited catalog of the IRAC Shallow Survey (ISS; Eisenhardt et al. 2004). Mass estimates were obtained for a subset of the ISCS clusters using X-ray emission, weak lensing measurements, or dynamical arguments (Brodwin et al. 2011; Jee et al. 2011; Andreon et al. 2011), as well as clustering analysis of the full ISCS sample (Brodwin et al. 2007).

Our goal is to observe actively star-forming cluster galaxies and to explore the future fate of these populations. Therefore, we only select spectroscopically confirmed cluster members from the Zeimann et al. (2013) catalog with the highest $H\alpha$ -based SFRs (i.e., $\gtrsim 120 M_{\odot}/\text{yr}$). This selection yields two galaxies with spectroscopic redshift of $z = 1.17$ belonging to the cluster ISCS J1426.5+3339 (Zeimann et al. 2013). The halo mass of ISCS J1426.5+3339 is expected to be in the range $\sim (0.8-2) \times 10^{14} M_{\odot}$, corresponding to a virial radius of ~ 1 Mpc (Wagner et al. 2015). Each of the two selected galaxies has $H\alpha$ -based $\text{SFR} \simeq 130 M_{\odot}/\text{yr}$. In Table 1 we report the properties of the two targets.

Neither of the targets is a plausible AGN candidate based on both infrared diagnostic and X-ray emission (Zeimann et al. 2013), as described in the following. The cluster ISCS J1426.5+3339 falls in fact within the X-ray XBoötes survey region (Kenter et al. 2005; Murray et al. 2005) and has deep Chandra observations (Martini et al. 2013) that enable the characterization of the AGN population of the cluster. AGN candidates within the sample of cluster galaxies of Zeimann et al. (2013) were identified and distinguished by the authors from star-forming galaxies either by means of their X-ray luminosities, or by adopting the empirical mid-infrared criteria by Stern et al. (2005). Sources matched to the Spitzer Deep Wide-Field Survey (SDWFS; Ashby et al. 2009) catalogs with signal-to-noise ratio $S/N > 5$ in all four IRAC bands that fall in the AGN edge of the diagnostic WISE color-color diagram by Stern et al. (2005) were also conservatively classified as AGNs by Zeimann et al. (2013).

We also checked that the two sources considered in this work are not included in the catalog of the Very Large Array Faint Images of the Radio Sky at Twenty-Centimeters (VLA FIRST) survey at 1.4 GHz (Becker et al. 1995). The detection limit of

the FIRST catalog is ~ 1 mJy (with a typical root mean square (rms) of 0.15 mJy). Post-pipeline radio maps have a resolution of ~ 5 arcsec. The two selected sources are therefore unresolved by VLA FIRST. Assuming the flux value of ~ 1 mJy as upper limit, we estimate an isotropic rest frame 1.4 GHz luminosity density $L_\nu < 7 \times 10^{31}$ erg s $^{-1}$ Hz $^{-1}$ associated with the blended emission from the two sources. A fiducial spectral index $\alpha = 0.8$ and the power-law $L_\nu \propto \nu^{-\alpha}$ are assumed for the calculation. The estimated upper limit implies that if the two target sources host radio galaxies, they have low non-thermal radio luminosities, compatible with galaxies populating the faint end of the radio luminosity function.

3. Observations and data reduction

We observed the two sources with eight antennas using the compact array D-configuration of the NOEMA interferometer (P.I.: Castignani). Such a configuration provides the lowest phase noise and the highest surface brightness sensitivity. It is therefore best suited for detection experiments such as ours. Our observations aim at detecting CO(2-1) from the two sources at observer frame frequency $\nu_{\text{obs}} = 106.239$ GHz (i.e., $\nu_{\text{rf}} = 230.538$ GHz in the rest frame), given the spectroscopic redshift $z = 1.17$ (Zeimann et al. 2013). At an angular resolution of ~ 3 arcsec, the two target sources are unresolved. The phase center of our observation is R.A. = 14h:26m:26.090s, Dec. = 33d:38m:27.600s, corresponding to the J2000 coordinates of the northernmost galaxy among the two (Zeimann et al. 2013). Figure 1 shows the HST images, taken with the WFC3/infrared camera (Kimble et al. 2008), of the two unresolved sources along with the NOEMA beam (bottom), as well as of the cluster field (top). The image at the top is centered at the cluster center coordinates, corresponding to the galaxy overdensity peak found using photometric redshifts of galaxies (Eisenhardt et al. 2008). We employed the WideX correlator which provides 3.6 GHz of instantaneous dual-polarization bandwidth. The observations were carried out over four days (15 Jul, 29 Jul, 3 Aug, and 6 Aug, 2017) in good to average weather conditions: radio seeing at ν_{obs} in the range $\sim (1.43 - 1.81)$ arcsec and precipitation water vapor in the range $\sim (3 - 15)$ mm. The on-source observing time is ~ 7.7 hr (12.3 hr in total, including overheads), corresponding to 987 scans. Data reduction was performed using the latest release of GILDAS package as of May 2017¹. Data were calibrated using standard pipeline adopting a natural weighting scheme to maximize sensitivity. Only minor flagging was required: 27 scans ($\lesssim 3\%$ of the total) were removed because of bad weather conditions during their acquisition.

4. Results

4.1. Significance of the detection

In Fig. 2 we present the results of our NOEMA observations where the detection of the two blended sources from the intensity map and the corresponding CO(2-1) spectrum at a resolution of 200 km/s are shown. Consecutive levels in the intensity map correspond to an increment and a decrement of 0.5 rms, starting from the values of +1 rms and -1 rms, respectively. The rms=0.9 mJy/beam-km/s is estimated here from the map, considering the region defined by relative coordinates, with respect

to those of J142626.1+333827, with absolute values in the range between 4 and 12 arcsec.

We fit the spectrum using the χ^2 minimization procedure with a best-fit model given by the sum of a Gaussian and a polynomial of degree one to account for the CO(2-1) spectral line and the baseline, respectively, as shown in Fig. 2 (right panel). The fit yields $\chi^2/\text{d.o.f.} = 1.39$, where d.o.f. is the number of degrees of freedom with five best fit parameters, that is, the intercept and the slope of the polynomial describing the baseline, as well as the normalization, the width, and the mean of the Gaussian. The fit yields a CO(2-1) peak flux of 0.34 mJy. The best fit is reported in the right panel of Fig. 2.

At 106.239 GHz, the field of view of NOEMA is ~ 50 arcsec (25 arcsec radius). We visually inspected both the archival HST image (Fig. 1) and the radio intensity map (Fig. 2) within the NOEMA field of view. No serendipitous detection of additional cluster, background, or foreground sources has been found.

To estimate both the significance of the detection and the uncertainties in the best fit parameters, we adopt criteria based on χ^2 statistics and perform Monte Carlo simulations, as described in the following. We derive the rms dispersion around the mean of the spectrum within the velocity range between 1,000 km/s and 7,000 km/s; this gives an estimate of the noise level equal to 79 μ Jy.

We then generate $N = 100,000$ simulated spectra assuming that at fixed velocity channel the flux value of each simulated spectrum is drawn from a Gaussian distribution with a mean equal to the observed flux at that velocity channel and a variance equal to the square of the estimated noise level. Then we fit each simulated spectrum with the χ^2 minimization procedure as described above. The resulting N fits are reasonably good, with $\chi^2/\text{d.o.f.} < 4$ for all of them.

We estimate the expected value as well as both the upper and lower uncertainties of each best fit parameter, as the median value of the corresponding distribution, and the values delimiting both the upper and lower 15.865% quartiles of the distribution, respectively. The statistical errors associated with the peak velocity and the width of the CO(2-1) line are estimated also with standard criteria based on χ^2 statistics (Cash 1976) applied to the observed spectrum. The estimated uncertainties are ~ 70 km/s, lower than the adopted channel width. Therefore, we consider the latter as fiducial uncertainty for both best fit parameters.

The resulting estimated full width at half maximum (FWHM) of the detected CO(2-1) line is (733 ± 200) km/s, which is large when compared to the typical width of ~ 200 -300 km/s. We refer to Sect. 5 for a discussion. The best fit peak velocity of the CO(2-1) line is translated into a redshift estimate z for the two unresolved sources. Our analysis yields $z = 1.163 \pm 0.001$, fully consistent within the uncertainties with that reported by Zeimann et al. (2013) using HST grism spectroscopy (see Table 1).

To assess the significance of the detection we estimate the integrated CO(2-1) fluxes using the Gaussian best fit model of each simulated spectrum. This procedure implies a velocity integrated CO(2-1) flux $S_{CO(2-1)\Delta v} = (0.27^{+0.06}_{-0.05})$ Jy km/s, where the reported value and errors are the median and the uncertainties within the 68.27% confidence region of the distribution of the integrated CO fluxes, as described above. The distribution is plotted in Fig. 3. The estimated flux and uncertainty imply that our detection has a S/N = 5.4. As a consistency check, we note that the mean values of both estimated flux and redshift found with Monte Carlo simulations are equal to those found from the best fit model of the observed spectrum. The fact that the two

¹ <https://www.iram.fr/IRAMFR/GILDAS/>

unresolved galaxies are detected in CO(2-1) by NOEMA both in projected space at the source coordinates and in frequency at the source redshift further supports the reliability of both our detection and the S/N estimate.

We stress that the noise associated with interferometric observations is not Gaussian in the projected space. In fact, spurious peaks due to the side lobes can occur at coordinates that are not coincident with the phase center of our observations, also considering the low S/N of the our detection. These aspects prevent us from estimating the S/N directly from the intensity map of Fig. 2a. Instead, similarly to previous work (Walter et al. 2016; Decarli et al. 2016), we need to rely on a positional prior: we cannot search for CO detections within the entire data cube (rms=0.3 mJy/beam at 100 km/s resolution) without relying on robust HST counterparts. Our target galaxies are in fact clearly detected (based on HST observations, Zeimann et al. 2013) in both redshift and projected coordinates, independently of our CO observations.

4.2. Molecular gas mass

We derive the CO(2-1) luminosity $L'_{CO(2-1)}$ for the two blended sources from the velocity integrated CO(2-1) line flux using Eq. (3) of Solomon & Vanden Bout (2005):

$$L'_{CO(2-1)} = 3.25 \times 10^7 S_{CO(2-1)} \Delta v v_{\text{obs}}^{-2} D_L^2 (1+z)^{-3}. \quad (1)$$

We obtain $L'_{CO(2-1)} = (4.9^{+1.1}_{-0.9}) \times 10^9 \text{ pc}^2 \text{ K km s}^{-1}$, typical of galaxies with infrared luminosities $\gtrsim 10^{11} L_{\odot}$; see, for example, Fig. 8 of Solomon & Vanden Bout (2005). Using $L'_{CO(2-1)}$ and standard relations we estimate a number of additional physical properties, as described in the following.

By assuming a Galactic CO-to-H₂ conversion factor $X_{CO} \simeq 2 \times 10^{20} \text{ cm}^{-1}/(\text{K km/s})$, that is, $\alpha_{CO} = 4.36 M_{\odot} (\text{K km s}^{-1} \text{ pc}^2)^{-1}$, typical of main sequence (MS) galaxies (Solomon et al. 1997; Bolatto et al. 2013), we estimate a total molecular gas mass of $M(\text{H}_2) = \alpha_{CO} L'_{CO(2-1)} = (2.2^{+0.5}_{-0.4}) \times 10^{10} M_{\odot}$ for the two blended sources. We note that the conversion factor α_{CO} is commonly used to convert $L'_{CO(1-0)}$ into $M(\text{H}_2)$, where $L'_{CO(1-0)}$ is the velocity integrated CO(1-0) luminosity. Therefore we implicitly assume fully excited gas in our calculation, that is, $r_{21} = L'_{CO(2-1)}/L'_{CO(1-0)} = 1$, typical of distant star-forming galaxies, or at least a fraction of them (Daddi et al. 2015, see also Sect. 5 for a discussion).

We stress here that we do not know the relative contribution of each of the two unresolved sources to the total CO(2-1) flux. Therefore we consider in the following the scenarios in which the observed flux is either due to one of the two sources or to both of them. Since the two galaxies have similar H α -based SFRs and equal stellar masses estimated by Zeimann et al. (2013) we will not be able to distinguish which of the two sources contributes more significantly to the observed CO(2-1) flux. We define as f the fraction of the observed CO(2-1) flux that is due to J142626.1+333827. Given such a notation, the two cases $f = 0$ and $f = 1$ are considered as indistinguishable. We consider in the following, when appropriate to estimate physical properties, the two extreme cases where $f = 0$ and $f = 1/2$, keeping in mind that the correct values will be intermediate between the two. Physical quantities related to $f = 1/2$ refer to either J142626.1+333827 or J142626.1+333826, considered individually. On the other hand, those related to $f = 0$ refer to only one of the two galaxies, assuming that this source contributes the total CO(2-1) flux.

4.3. Star formation rate

We exploit our observations to estimate the SFR independently from Zeimann et al. (2013) by using Spitzer MIPS observations in the mid-infrared. We search for our sources in the Spitzer Enhanced Imaging Products (SEIP) source catalog². A Spitzer MIPS detection at 24 μm in the observer frame is found at an angular separation of 1.44 and 0.72 arcsec from J142626.1+333826 and J142626.1+333827, respectively. Our target sources are unresolved by Spitzer MIPS, given its angular resolution of ~ 6 arcsec at 24 μm , corresponding to the FWHM of the telescope point spread function. The 24 μm flux of the Spitzer MIPS source is $(2.755 \pm 0.122) \times 10^2 \mu\text{Jy}$ that we use to estimate the SFR. We use a procedure analogous to that adopted by McDonald et al. (2016). We estimate the $\lambda = 24 \mu\text{m}$ rest frame luminosity λL_{λ} by assuming a power-law model, $L_{\lambda} \propto \lambda^{\gamma}$, with $\gamma = 2.0 \pm 0.5$ (Casey 2012). We incorporate the uncertainties in both γ and the observed 24 μm flux by using $M = 100,000$ values drawn from Gaussian distributions centered at the mean values and with standard deviations equal to the reported uncertainties. Then we use the Calzetti et al. (2007) relation to convert the 24 μm rest frame luminosity into an estimate of the SFR. This procedure yields $\text{SFR}(24\mu\text{m}) = (52^{+21}_{-15}) M_{\odot}/\text{yr}$ ($f = 0$) and $\text{SFR}(24\mu\text{m}) = (28^{+12}_{-8}) M_{\odot}/\text{yr}$ ($f = 1/2$). The reported SFR values and uncertainties are the medians and the 68.27% confidence levels estimated from the M realizations, respectively. The notation (24 μm) refers to the fact that the SFR is estimated using 24 μm fluxes.

Taking the uncertainties in the SFR estimates into account, the SFR(24 μm) is marginally consistent with the H α -based SFR = $(127^{+100}_{-75}) M_{\odot}/\text{yr}$ and $(134^{+100}_{-75}) M_{\odot}/\text{yr}$, estimated by Zeimann et al. (2013) for the galaxies J142626.1+333827 and J142626.1+333826, respectively (see Table 1). Therefore, we suspect that AGN emission might contribute to the observed H α flux, which results in H α -based SFRs that are possibly biased-high (see also Sect. 5). For this reason, we henceforth adopt the SFR(24 μm) as SFR estimate for our target galaxies. No evidence for AGN contamination has been found for our target galaxies using mid-infrared criteria by previous work (see Sect. 2). However, we stress here that a possible contamination cannot be excluded at 24 μm , that is, 11 μm in the rest frame, where AGN contribution is however typically limited to $\lesssim 20\%$ for distant star-forming galaxies (Donley et al. 2012; Pozzi et al. 2012; Delvecchio et al. 2014).

We also note that the two scenarios of $f = 0$ and $f = 1/2$ have been introduced for the CO emission. By applying the same f -prescription for the estimate of the SFR(24 μm) we implicitly assume that the CO emission correlates well with that at 24 μm . This assumption and our choice for the SFR is strengthened by the fact that the SFR(24 μm) fully agrees with that expected from standard L'_{CO} versus SFR relations, such as that found by Daddi et al. (2010) between the L'_{CO} and the infrared luminosity for both MS and color-selected star-forming galaxies at $z \sim 0.5-2.3$. We refer to Carilli & Walter (2013) for a review. By using the relation of Daddi et al. (2010) and that of Kennicutt (1998a) between the total far-infrared luminosity and the SFR, we obtain $\text{SFR}(\text{CO}) = (52^{+33}_{-32}) M_{\odot}/\text{yr}$ and $\text{SFR}(\text{CO}) = (24 \pm 15) M_{\odot}/\text{yr}$ for $f = 0$ and $f = 1/2$, respectively. The reported uncertainties take into account those associated with the estimated CO(2-1) luminosity that are summed in quadrature to fiducial $\sim 58\%$, that is, 0.25 dex, uncertainties associated with the calibration and the

² <https://irsa.ipac.caltech.edu/data/SPITZER/Enhanced/SEIP/overview.html>

scatter of the adopted scaling relations (Daddi et al. 2010). The notation (CO) refers to the fact that the SFR is estimated by exploiting CO observations. We note that the relations used to estimate the SFR from the molecular gas properties are ultimately related to the Kennicutt-Schmidt law (Schmidt 1959; Kennicutt 1998b) which links the molecular gas density to the SFR density, whereas the integrated CO(2-1) flux that is used here to estimate the molecular gas content is not a *direct* tracer of star formation.

4.4. Main sequence and depletion time

We use the stellar mass $\text{Log}(M_\star/M_\odot) = 10.8 \pm 0.5$ reported by Zeimann et al. (2013) for each of two considered galaxies to estimate a number of physical parameters, as described in the following. Our results imply a specific star formation rate $\text{sSFR}(24\mu\text{m}) = \text{SFR}(24\mu\text{m})/M_\star = (0.82^{+0.65}_{-0.64}) \text{Gyr}^{-1}$ and $(0.44^{+0.36}_{-0.34}) \text{Gyr}^{-1}$ in the case of $f = 0$ and $f = 1/2$, respectively. The reported uncertainties are obtained by taking those associated with both $\text{SFR}(24\mu\text{m})$ and M_\star into account.

By exploiting the SFR values above, we also estimate a depletion timescale associated with the consumption of the molecular gas, equal to $\tau_{\text{dep}} = M(\text{H}_2)/\text{SFR}(24\mu\text{m}) = (4.2^{+1.6}_{-1.9}) \times 10^8 \text{yr}$ and $(3.9^{+1.4}_{-1.8}) \times 10^8 \text{yr}$ for $f = 0$ and $f = 1/2$, respectively. The reported uncertainties are obtained by propagating and combining in quadrature those associated with the SFR and $M(\text{H}_2)$. For the sake of clarity, we also derive and report in Table 1 the depletion time, as well as the $\text{sSFR}(\text{H}\alpha)$, estimated by adopting $\text{SFR}(\text{H}\alpha)$. The notation (H α) refers to the fact that the H α -based SFR is used. We obtain $\tau_{\text{dep}}(\text{H}\alpha) = M(\text{H}_2)/\text{SFR}(\text{H}\alpha) = (0.87^{+0.55}_{-0.70}) \times 10^8 \text{yr}$ and $(0.82^{+0.49}_{-0.63}) \times 10^8 \text{yr}$ in the case $f = 1/2$, for J142626.1+333827 and J142626.1+333826, respectively. The reported uncertainties are estimated by summing in quadrature those associated with both $\text{SFR}(\text{H}\alpha)$ and $M(\text{H}_2)$.

Furthermore, we estimate the molecular gas to stellar mass ratio $M(\text{H}_2)/M_\star$, equal to $0.35^{+0.25}_{-0.26}$ and 0.17 ± 0.13 for $f = 0$ and $f = 1/2$, respectively. The reported uncertainties are estimated by taking those associated with both $M(\text{H}_2)$ and M_\star into account. We refer to Sect. 5 for a discussion.

4.5. Continuum emission and dust mass

Our observations did not allow us to detect the continuum flux. However, we exploit them to derive an upper limit on the dust mass of the two blended galaxies.

We estimate a $3\text{-}\sigma$ upper limit of $33 \mu\text{Jy}$ for the continuum flux $S_{\nu_{\text{obs}}}$ of the two blended sources at the observed frequency ν_{obs} , within the 3.6 GHz bandwidth of WideX. The estimate is consistent with that inferred by assuming a standard dependence of the rms on the inverse of the square root of the bandwidth. Following previous work (e.g., Beelen et al. 2006), the continuum flux can be expressed as a function of the dust mass M_{dust} :

$$S_{\nu_{\text{obs}}} = \frac{1+z}{D_L^2} M_{\text{dust}} \kappa(\nu_{\text{rf}}) B_{\nu_{\text{rf}}}(\nu_{\text{rf}}, T_d), \quad (2)$$

where z is the redshift of the two selected galaxies, $\kappa(\nu)$ is the dust opacity per unit mass of dust, and $B_\nu(\nu, T)$ is the spectral radiance of a black body of temperature T at frequency ν . It holds:

$$B_\nu(\nu, T) = \frac{2h\nu^3}{c^2} \frac{1}{e^{h\nu/k_B T} - 1}, \quad (3)$$

where h is the Planck constant, c is the speed of light, and k_B is the Boltzmann constant. We assume dust temperature $T_d =$

25 K, following recent work by Scoville et al. (2017) on a large sample of ~ 700 distant galaxies with ALMA detections within the redshift range $z = 0.3 - 4.5$.

We also model the dust opacity as $\kappa(\nu) = \kappa_0(\frac{\nu}{\nu_0})^\beta$, with $\kappa_0 = 0.4 \text{cm}^2 \text{g}^{-1}$, $\nu_0 = \frac{c}{1200\mu\text{m}}$ (Beelen et al. 2006; Alton et al. 2004, and references therein), and $\beta = 1.8$ (Scoville et al. 2017). In particular, the value chosen for β is based on the determinations for our Galaxy from Planck (Planck Collaboration 2011a,b). We refer to Berta et al. (2016) and Bianchi (2013) for a discussion on possible variations in β . These assumptions yield a $3\text{-}\sigma$ upper limit for the total dust mass of the two blended sources, $M_{\text{dust}} < 4.2 \times 10^8 M_\odot$, consistent with dust reservoirs found for MS galaxies (Berta et al. 2016).

4.6. Effective radii

We also use SExtractor (Bertin & Arnouts 1996) to estimate the size of our target galaxies from the HST image reported in Fig. 1. We derive effective radii $R_e \simeq (3 - 4) \text{kpc}$, where the point spread function has been taken into account by convolving the HST image with a Gaussian filter with a FWHM=2 pixels, corresponding to $\sim 2 \text{kpc}$ at the redshift of our target galaxies. The results are summarized in Tables 1 and 2.

4.7. Molecular gas properties of cluster galaxies at $0.2 \lesssim z \lesssim 2.0$

We compare the results found for our galaxies in terms of molecular gas content, SFR, and depletion time with those found by other studies, including recent ones, of both MS field galaxies and distant cluster galaxies, over a broad redshift range $0.2 \lesssim z \lesssim 2.0$, corresponding to $\sim 7.8 \text{Gyr}$ of cosmic time.

Similarly to Noble et al. (2017), we exploit recent observations of CO in cluster galaxies to study the evolution of the molecular gas content. We include CO detections of cluster galaxies at $z \sim 0.2$ (Cybulski et al. 2016), $z \sim 0.4 - 0.5$ (Geach et al. 2011; Jablonka et al. 2013); $z \sim 1.1$ (Wagg et al. 2012), and $z \sim 1.5 - 1.6$ (Aravena et al. 2012; Noble et al. 2017). We also include more recent results from Rudnick et al. (2017), Webb et al. (2017), and Hayashi et al. (2018) at $z \sim 1.5 - 1.7$ and those from Coogan et al. (2018) at $z \simeq 2.0$, as well as our CO(2-1) detection. This yields 55 sources over 15 clusters, including our detection, counted here as a single source, with available estimates of the SFR and both stellar and total gas masses. Among the sources, we include two pairs of unresolved galaxies from Noble et al. (2017), namely J0225-3680/3624 and J0225-396/424. Consistently with Noble et al. (2017), we count them as single sources and adopt physical quantities reported in their Table 1 for each of the two pairs. We note that the work by Hayashi et al. (2018), published after the submission of the present paper, reports 17 galaxies detected in CO belonging to the cluster XMMXCS J2215.9-1738 at $z = 1.5$. Their work includes CO results from Hayashi et al. (2017). The sample of Stach et al. (2017) comprising six sources with independent CO detections from the same cluster is also entirely included in Hayashi et al. (2018). Therefore, concerning XMMXCS J2215.9-1738 cluster galaxies, we consider their more recent results.

In Fig. 4, we show the fractional offset from the star-forming MS as a function of the molecular gas depletion timescale (left) and molecular gas to stellar mass ratio (right), where we limit ourselves to galaxies with estimated stellar mass $> 10^{10} M_\odot$. For each galaxy, we also require $\text{SFR} < 6 \text{SFR}_{\text{MS}}$, where SFR_{MS}

is the SFR estimated using the Speagle et al. (2014) model for MS field galaxies of stellar mass and redshift equal to those of the galaxy considered. This selection yields 49 sources over the 15 clusters, shown in Fig. 4. In Fig. 5, we show the evolution of the molecular gas to stellar mass ratio for the same 49 cluster galaxies. In the left and right panels of Fig. 4, the x-axis values τ_{dep} and $M(\text{H}_2)/M_\star$ are rescaled by $(1+z)^{B_t}$ and $\eta(z)$, respectively, to take the redshift dependence inferred by Tacconi et al. (2018) into account, where $B_t = -0.62$ and $\text{Log } \eta(z) = -3.62 \times [\text{Log}(1+z) - 0.66]^2$. When needed, we corrected the molecular mass estimates from the literature to take the different conversion factors α_{CO} into account. We assume $\alpha_{\text{CO}} = 4.36 M_\odot (\text{K km s}^{-1} \text{pc}^2)^{-1}$, consistently with the value adopted throughout this work, while for each galaxy we assume the excitation level adopted in the corresponding work. We stress that by assuming the same α_{CO} for all galaxies, we only aim at having comparable molecular gas content for the galaxies considered; according to our selection, the majority of them lie around the MS, which justifies our choice for α_{CO} , as further described in the following.

Coogan et al. (2018) reported CO line fluxes for eight cluster galaxies, six of them also have stellar mass estimates and are considered in this work. All six sources are detected in CO(4-3) while two of them are also detected in CO(1-0). To estimate the molecular gas mass, we used the CO(1-0) flux, when available. Alternatively, we used the CO(4-3) flux by assuming an excitation level $r_{41} = L'_{\text{CO}(4-3)}/L'_{\text{CO}(1-0)} = 0.36$ equal to the mean value inferred from the two galaxies with both CO(1-0) and CO(4-3) detections.

As noted by Noble et al. (2017), including galaxies significantly above the MS might lead to biased-high molecular gas to stellar mass ratios. Such sources are also typically associated with lower values for α_{CO} . Among the 49 sources considered in Figs. 4 and 5, those that have $\text{SFR} > 3 \times \text{SFR}_{\text{MS}}$ are mainly at $z < 0.6$, with the only exceptions represented by the galaxy at $z \approx 1.7$ of Webb et al. (2017), the galaxy with ID number 51858 of Aravena et al. (2012), at $z \approx 1.6$, the sources ALMA.12 and ALMA.17 at $z \approx 1.5$ of Hayashi et al. (2018) (see their Table 2), and the source at $z \approx 1.1$ of Wagg et al. (2012). Concerning the last one, we note that their estimated $\text{SFR} < 150 M_\odot/\text{yr}$ is an upper limit due to the likely AGN contamination (Wagg et al. 2012). For the sake of completeness we do not reject these galaxies. This choice will not affect our conclusions.

In Figs. 4 and 5, the uncertainties of τ_{dep} and $M(\text{H}_2)/M_\star$ for the sources with CO detections from the literature are estimated considering M_\star , $M(\text{H}_2)$, and SFR as independent variables. In particular, we checked that the SFRs from the literature used in this work are indeed independent from the associated CO observations and are based on spectral energy distribution (SED) fitting (Aravena et al. 2012; Noble et al. 2017; Rudnick et al. 2017), infrared luminosity (Wagg et al. 2012; Jablonka et al. 2013; Cybulski et al. 2016; Stach et al. 2017; Webb et al. 2017), and polycyclic aromatic hydrocarbon 7.7 μm emission (Geach et al. 2011). Hayashi et al. (2018) provide SFR estimates obtained using either i) SED fitting to the optical-to-mid-infrared photometry or ii) a combination of ultraviolet and infrared luminosities. We adopted the latter when both SFR estimates are available for a given source of their sample, analogously to what has been done by the authors. However, we stress that for the six sources of Stach et al. (2017) included in Hayashi et al. (2018), the SFRs from the two studies are discrepant up to a factor of ~ 5 in some cases, which is due to the high uncertainties typically associated with SFR estimates (see also Sect. 5). Coogan et al. (2018) report SFR estimates derived from the CO(4-3),

1.4 GHz, or 870 μm fluxes. We adopted the SFR estimates based on the 870 μm fluxes.

5. Discussion

5.1. Main sequence, star formation, and depletion time

Our results based on CO(2-1) observations show that the two unresolved galaxies have both SFR and sSFR consistent with those of MS galaxies; see, for example, our Fig. 4, and Fig. 7 of Zeimann et al. (2013). These conclusions are valid for both presented scenarios where either $f = 0$ or $f = 1/2$, and where the SFR(24 μm) is adopted. Our results are also fairly consistent with those found by considering instead the SFR($\text{H}\alpha$) from Zeimann et al. (2013), given the large uncertainties associated with the physical quantities such as SFR, M_\star , and $M(\text{H}_2)$; see Tables 1 and 2.

In the case where $f = 1/2$, that is, where both sources contribute equally to the observed CO(2-1) flux, the SFR(24 μm) is $\sim 1/5$ SFR($\text{H}\alpha$), for each of the two galaxies, separately. SFR estimates can be in fact uncertain by a factor of ~ 2 or higher (e.g., Kobayashi et al. 2013). This is mainly due to the scatter between the SFR and SFR indicators such as the $\text{H}\alpha$ luminosity and to the specific physical assumptions such as those adopted in this work. For our two target sources, the discrepancy between SFR(24 μm) and SFR($\text{H}\alpha$) is still fairly compatible with the estimated uncertainties. However, even if no AGN contribution was found by previous work (e.g., Zeimann et al. 2013), as noted in Sect. 4, some AGN contamination might occur, resulting in biased-high SFR($\text{H}\alpha$) estimates. Such a scenario could favor a better agreement between the SFR($\text{H}\alpha$) and the SFR(24 μm).

The depletion time of our target galaxies $\tau_{\text{dep}} \sim 0.4$ Gyr is marginally consistent with, but shorter than that of MS galaxies. In fact, the model of Tacconi et al. (2018) predicts, for MS field galaxies, a higher depletion time than that estimated for our target galaxies. The value $\tau_{\text{dep}} \approx (0.8 \pm 0.1)$ Gyr is found for MS field galaxies of stellar mass and redshift similar to those of our target sources (see Fig. 4). The uncertainties associated with the adopted physical assumptions may explain such a τ_{dep} discrepancy. In particular, we assumed fully excited gas. However, if the excitation level is lower, that is, $r_{21} < 1$, we could have higher values of $M(\text{H}_2)$ and, consequently, a higher τ_{dep} .

A number of observational facts privilege the scenario where both target galaxies contribute to the observed CO(2-1) emission implying that the case where $f = 1/2$ might be more realistic than $f = 0$. The two galaxies have in fact similar stellar masses and $\text{H}\alpha$ -based SFRs, as found in previous work (Zeimann et al. 2013). Furthermore the FWHM of the detected CO(2-1) line is ~ 700 km/s which is large when compared to the typical width of ~ 200 -300 km/s found for cluster galaxies at similar redshift (e.g., Noble et al. 2017; Rudnick et al. 2017, and references therein). Such a discrepancy suggests that the two galaxies might have a large relative velocity of ~ 400 km/s and that the observed CO(2-1) emission is indeed coming from both target galaxies.

The fact that the two galaxies have a projected angular separation of 6 kpc and are not resolved in velocity by their CO(2-1) spectrum might also suggest that the two sources are in a pair. However, cluster galaxies can have large peculiar velocities, up to $\sim 2,000$ km/s for rich clusters (e.g., Sheth & Diaferio 2001; Biviano et al. 2013). Therefore we cannot exclude the possibly that projection effects occur and that the 3D physical separation between the two target galaxies is large.

Since the two sources have molecular gas content and sSFR compatible with those of MS galaxies we suggest that they are

not yet interacting. Alternatively, under the assumption that they are in a pair, their interaction has not yet led to their starburst phase. Since the two galaxies are not resolved by our NOEMA observations, we cannot distinguish between different gas processing mechanisms (e.g., gas stripping).

5.2. Future perspectives

Higher-resolution and higher-frequency observations at millimeter wavelengths will enable us to deblend the two sources both in velocity and in projected space. The presence/absence of asymmetries or disturbed morphology could be used to distinguish between different gas processing mechanisms. The spatial distribution of the CO emission, in particular, will allow us to understand if CO is confined within each galaxy or if it is associated with a more extended emission connecting the two galaxies. If the latter scenario is confirmed, the two sources may be interacting. Such interaction may lead to a starburst phase by $z \sim 0$, as observed for example in local major merging gas-rich pairs such as the Antennae Galaxies (Gao et al. 2001; Ueda et al. 2012; Whitmore et al. 2014).

Higher-resolution observations of higher-J CO transitions such as CO(4-3) could also be used to better estimate both the continuum flux and the dust mass in the Rayleigh-Jeans regime, as well as probe the excitation level, in combination with the CO(2-1) detection presented in this work.

5.3. Comparison with other distant cluster galaxies

The data available from the literature on the SFR and depletion time of $z > 1$ cluster galaxies (Fig. 4) are in overall agreement with the model of field galaxies. Similarly, the molecular gas to stellar mass ratio (Fig. 5) is fairly consistent with model predictions of MS galaxies in the field, given the dispersion in data points and the uncertainties underlying the physical assumptions such as those of the α_{CO} conversion factor, and of both SFR and stellar mass estimates. However, as also noted in Noble et al. (2017) on the basis of their CO observations and those prior to 2017, the molecular gas to stellar mass ratio of $z > 1$ cluster galaxies from the literature seems to be generally higher than that of field galaxies. This statement does not apply to either our galaxies or recent CO observations of cluster galaxies at $z \sim 1.6$ and $z \sim 2.0$ from Rudnick et al. (2017) and Coogan et al. (2018), respectively. Increasing the sample of distant CO detected cluster galaxies will certainly help to achieve a better understanding of their statistical molecular gas properties.

The fact that the two target galaxies have molecular gas mass and depletion times that are marginally compatible with but smaller than those of MS field galaxies suggests that the molecular gas has not been adequately refueled. We speculate that the cluster environment might have played a role in preventing the refueling via environmental mechanisms such as galaxy harassment, strangulation, ram-pressure, or tidal stripping.

5.4. Additional comments on physical assumptions and models

Some additional comments are needed concerning the physical assumptions and conventions adopted in this work. The exact value of the H₂-to-CO conversion factor is unknown. By assuming a lower $\alpha_{CO} \simeq (1 - 2) M_{\odot}(\text{K km s}^{-1} \text{ pc}^2)^{-1}$ (Wagg et al. 2012; Stach et al. 2017; Webb et al. 2017), typical of (ultra-) luminous infrared galaxies (Bolatto et al. 2013), we find shorter

depletion time scales and smaller molecular gas to stellar mass ratios for the two selected galaxies, which imply a stronger discrepancy with respect to the values found for MS field galaxies. These findings further support our choice for α_{CO} . Furthermore, as noted above, if the excitation level were found to be lower than assumed, that is, $r_{21} < 1$, we would obtain higher molecular gas to stellar mass ratios and higher depletion time scales, leading to a better agreement with respect to the model for MS galaxies.

We also stress here that the stellar mass estimates used in this work to infer quantities such as $M(\text{H}_2)/M_{\star}$ and sSFR rely on stellar population synthesis models and have statistical uncertainties $\sim (0.10 - 0.14)$ dex (e.g., Roediger & Courteau 2015). Additional ~ 0.25 dex uncertainty may be added because of the unknown initial mass function (Wright et al. 2017, and references therein). This yields a typical uncertainty of ~ 0.3 dex on the stellar mass. Our two target galaxies have stellar masses with estimated uncertainties that are even higher and equal to ~ 0.5 dex; see Table 1. Stellar masses of our two target galaxies have been estimated by Zeimann et al. (2013) using a Chabrier (2003) initial mass function.

We note that both the depletion time and the molecular gas to stellar mass ratio only weakly depend on the effective radius R_e . Tacconi et al. (2018) found that both τ_{dep} and $M(\text{H}_2)/M_{\star}$ scale as $\propto (R_e/R_{e0})^{0.11}$, where $R_{e0} = 8.9 \text{ kpc} (1+z)^{-0.75} [M_{\star}/(5 \times 10^{10} M_{\odot})]^{0.22}$ is the mean effective radius of star-forming galaxies as a function of z and M_{\star} from van der Wel et al. (2014). For our two target sources, we have $R_e \simeq 3\text{-}4 \text{ kpc}$ and $R_{e0} = 5.2 \text{ kpc}$, which implies a negligible correction of $\lesssim 5\%$ on the model values of τ_{dep} and $M(\text{H}_2)/M_{\star}$, that are reported in Figs. 4 and 5 in the case of $R_e = R_{e0}$.

We also checked that our results are fairly independent of the specific model used for MS field galaxies. We adopted the model prescriptions described by Tacconi et al. (2018) whose study supersedes the previous one by Genzel et al. (2015). In particular, we used the Speagle et al. (2014) model for the SFR_{MS}, also used by Tacconi et al. (2018). Adopting instead the model by Whitaker et al. (2012) used by Genzel et al. (2015) would lead to a similar SFR_{MS}, only slightly higher by $(19 \pm 20)\%$ on average, well within the typical SFR uncertainties, where the reported value is the median value estimated from the data points reported in Fig. 4 and the uncertainty is the rms around the median. If we limit ourselves to galaxies with redshift and stellar mass equal to those of our target galaxies and if we use the Genzel et al. (2015) model prescriptions for star-forming galaxies τ_{dep} and $M(\text{H}_2)/M_{\star}$ are $\sim 20\%$ higher than those obtained using the model prescriptions by Tacconi et al. (2018). The Genzel et al. (2015) and Tacconi et al. (2018) models are therefore compatible with each other within the associated uncertainties. We refer to Tacconi et al. (2018) for a discussion.

6. Conclusions

In this work, we report a CO(2-1) detection (S/N = 5.4) from two unresolved cluster galaxies at $z = 1.2$, obtained with the IRAM NOEMA interferometer. The two galaxies are separated by 6 kpc in the projected space and are located at a projected radial distance of 500 kpc from the center of the distant cluster ISCS J1426.5+3339.

The two sources are selected as the ones with the highest SFR(H α), that is, $\gtrsim 120 M_{\odot}/\text{yr}$, within the Zeimann et al. (2013) catalog of $1.0 < z < 1.5$ cluster galaxies. The galaxies in this catalog belong to a total of 18 clusters from the Irac Shallow Cluster Survey (ISCS, Eisenhardt et al. 2004; Brodwin et al.

2006). The halo mass of the cluster ISCS J1426.5+3339, which the two selected galaxies belong to, is expected to be in the range $\sim (0.8-2) \times 10^{14} M_{\odot}$, corresponding to a virial radius of ~ 1 Mpc (Wagner et al. 2015).

The CO detection presented in this work is the first detection resulting from a wider search of molecular gas in distant cluster galaxies. It is also the first one from $1 < z < 1.4$ cluster galaxies with no reported clear evidence of AGNs.

Our observations yield an improvement, by a factor of ten in accuracy, of an unknown weighted mean of the redshifts of the two sources, $z = 1.163 \pm 0.001$, based on the CO(2-1) emission line peak. Our redshift estimate is also consistent with those obtained for the two target galaxies using the HST WFC3 camera and the near-infrared grism G141 (Zeimann et al. 2013).

The integrated CO(2-1) line luminosity implies a total molecular gas mass $M(\text{H}_2) = (2.2^{+0.5}_{-0.4}) \times 10^{10} M_{\odot}$ for the two blended sources. A Galactic CO-to- H_2 conversion factor $\alpha_{\text{CO}} = 4.36 M_{\odot} (\text{K km s}^{-1} \text{ pc}^2)^{-1}$ is used for the calculation. We also assumed fully excited gas.

The FWHM of the detected CO(2-1) line is ~ 700 km/s which is large when compared to the typical width of ~ 200 - 300 km/s found for cluster galaxies at similar redshift (e.g., Noble et al. 2017; Rudnick et al. 2017, and references therein). Such discrepancy suggests that the two galaxies might have a large relative velocity of ~ 400 km/s and that the observed CO emission indeed originates from both galaxies. However, since the two galaxies are not resolved by our NOEMA observations we cannot distinguish between different gas processing mechanisms (e.g., gas stripping).

By assuming that both blended sources contribute equally to the observed CO(2-1) and $24\mu\text{m}$ (Spitzer MIPS) emission, we estimate the $\text{SFR}(24\mu\text{m}) = (28^{+12}_{-8}) M_{\odot}/\text{yr}$, the depletion timescale $\tau_{\text{dep}} = (3.9^{+1.4}_{-1.8}) \times 10^8$ yr, and the molecular gas to stellar mass ratio $M(\text{H}_2)/M_{\star} = 0.17 \pm 0.13$, for each of the two galaxies.

The $\text{SFR}(24\mu\text{m})$ is consistent with that inferred from standard scaling relations involving molecular gas content (e.g., Daddi et al. 2010) and is $\sim 1/5$ $\text{SFR}(\text{H}\alpha)$. This result suggests that the $\text{SFR}(\text{H}\alpha)$ might be biased-high, possibly due to some AGN contamination. Nevertheless, the two SFR estimates are marginally consistent with each other within their uncertainties. The depletion time of our target galaxies is marginally consistent with but shorter than that of MS galaxies of stellar mass and redshift similar to those of our target sources, $\tau_{\text{dep}} \approx (0.8 \pm 0.1)$ Gyr (Tacconi et al. 2018).

Nevertheless, given the uncertainties associated with both model predictions and observations, the SFR , the molecular gas mass, and the depletion time of our target galaxies are in overall agreement with those found for other distant cluster galaxies at similar redshifts and with the model from Tacconi et al. (2018) for MS field galaxies of similar mass and redshift of our two sources. These results suggest that the two galaxies are not interacting, but are possibly close to interacting. Alternatively, their interaction has not led to their starburst phase yet. Such a starburst phase may be reached by $z \sim 0$, as observed, for example, in local major merging gas-rich pairs such as the Antennae Galaxies.

However, the fact that the two target galaxies have molecular gas mass and depletion time that are marginally compatible with but smaller than those of MS field galaxies suggests that the molecular gas has not been adequately refueled. We speculate that the cluster environment might have played a role in preventing the refueling via environmental mechanisms such as galaxy harassment, strangulation, ram-pressure, or tidal stripping.

Higher-resolution and higher-J CO observations at millimeter wavelengths will allow us to spatially resolve the two sources and possibly distinguish between different gas processing mechanisms.

Acknowledgements. This work is based on observations carried out under project number S17BJ with the IRAM NOEMA Interferometer. IRAM is supported by INSU/CNRS (France), MPG (Germany) and IGN (Spain). GC thanks Cinthya Herrera (LOC at NOEMA, Grenoble) and all IRAM staff for the hospitality in Grenoble and precious help concerning data reduction. We thank the anonymous referee for helpful comments that led to a substantial improvement of the paper. GC thanks Paola Dimauro for the help concerning the use of SExtractor. CC acknowledges funding from the European Union's Horizon 2020 research and innovation program under the Marie Skłodowska-Curie grant agreement No. 664931.

References

- Alberts, S. et al. 2016, ApJ, 825, 72
 Alton, P. B., Xilouris, E. M., Misiriotis, A. et al., 2004, A&A, 425, 109
 Andreon, S. et al. 2006, MNRAS, 365, 915
 Andreon, S. et al. 2011, MNRAS, 412, 2391
 Aravena, M., Carilli, C. L. et al. 2012, MNRAS, 426, 258
 Ashby, M. L. N., Stern, D., Brodwin, M., et al. 2009, ApJ, 701, 428
 Bai, L., et al. 2009, ApJ, 693, 1840
 Becker, R. H., White, R., & Helfand, D. J., 1995, ApJ, 450, 559
 Beelen, A., Cox, P., Benford, D. J. et al. 2006, ApJ, 642, 694
 Berta, S., Lutz, D. et al. 2016, A&A, 587, A73
 Bertin, E. & Arnouts, S., 1996, A&AS, 117, 393
 Bianchi, S. 2013, A&A, 552, A89
 Biviano, A., Rosati, P., Balestra, I. et al. 2013, A&A, 558, 1
 Bolatto, A. T. et al. 2013, ARA&A, 51, 207
 Brodwin, M., Brown, M. J. L., Ashby, M. L. N., et al. 2006, ApJ, 651, 791
 Brodwin, M., Gonzalez, A. H., Moustakas, L. A., et al. 2007, ApJL, 671, L93
 Brodwin, M., Stern, D., Vikhlinin, A., et al. 2011, ApJ, 732, 33
 Brodwin, M. et al. 2013, ApJ 779, 138
 Butcher H. & Oemler, A. 1984, ApJ, 285, 426
 Calzetti, D., Kennicutt, R. C. et al. 2007, ApJ, 666, 870
 Carilli, C. L., & Walter, F. 2013, ARA&A, 51, 105
 Casasola, V., Magrini, L., Combes, F. et al. 2013, A&A, 558, 60
 Casey, C. M. 2012, MNRAS, 425, 3094
 Cash, W. 1976, A&A, 52, 307
 Chabrier, G. 2003, PASP, 115, 763
 Chiang, Y.-K., Overzier, R. A. et al. 2017, ApJ, 844, 23
 Chung, A., van Gorkom, J. H., Kenney, J. D. P. et al., 2009, AJ 138, 1741
 Chung, S. M., et al. 2010, ApJ, 725, 153
 Coogan, R. T., Daddi, E. et al. 2018, arXiv:180509789
 Cybulski, R., 2016, MNRAS, 459, 3287
 Daddi E, Elbaz D, Walter F, Bournaud F, Salmi F, et al. 2010. ApJL, 714, 118
 Daddi, E., Dannerbauer, H., Liu, D. et al. 2015, A&A, 577, 46
 Decarli, R., Walter, F. et al. 2016, ApJ, 833, 70
 Delvecchio, I., Gruppioni, C. et al. 2014, MNRAS, 439, 2736
 Dekel, A., Birnboim, Y. et al. 2009a, Nature, 457, 451
 Dekel, A., Sari, R. et al. 2009b, ApJ, 703, 785
 Donley, J. L., Koekemoer, A. M. et al. 2012, ApJ, 748, 142
 Dressler, A. 1980, ApJ, 236, 351
 Eisenhardt, P. R., Stern, D., Brodwin, M., et al. 2004, ApJS, 154, 48
 Eisenhardt, P. et al. 2008, ApJ, 684, 905
 Emonts B. H. C., Lehnert, M. D. et al. 2016, Science, 354, 1128
 Gao, Y., Lo, K. Y. et al. 2001, ApJ, 548, 172
 Geach, J. E. et al., 2011, ApJL, 730, L19
 Genzel, R., Tacconi, L. J., Lutz, D. et al. 2015, ApJ, 800, 20
 Gunn, J. E. & Gott, J. R. III, 1972, ApJ, 176, 1
 Hayashi, M., Kodama, T., Kohno, K. et al. 2017, ApJ, 841, 21
 Hayashi, M., Tadaki, K. et al. 2018, ApJ, 856, 118
 Jablonka, P., 2013, A&A, 557, 103
 Jáchym, P., Combes, F. et al., 2014, ApJ, 792, 11
 Januzzi, B. T., & Dey, A. 1999, in ASP Conf. Ser. 191, Photometric Redshifts and the Detection of High Redshift Galaxies, ed. R. Weymann, L. Storrie-Lombardi, M. Sawicki, & R. Brunner (San Francisco, CA: ASP), 111
 Jee, M. J., Dawson, K. S., Hoekstra, H., et al. 2011, ApJ, 737, 59
 Kauffmann, G., 2004, MNRAS, 353, 713
 Kennicutt, R. C. J., 1998a, ARAA, 36, 189
 Kennicutt, R. C. J., 1998b, ApJ, 498, 2, 541
 Kenter, A., Murray, S. S., Forman, W. R., et al. 2005, ApJS, 161, 9
 Kimble, R. A., MacKenty, J. W., et al. 2008, Proc. SPIE, 7010, 43

- Kobayashi, M. A. R. et al., 2013, *ApJ*, 763, 3
Kodama, T. et al., 2001, *ApJ*, 562, 9
Larson, R. B. et al. 1980, *ApJ*, 237, 69
Madau, P. & Dickinson, M., 2014, *ARA&A*, 52, 415
Mancone, C. L., et al. 2010, *ApJ*, 720, 284
Martini, P., Miller, E. D., Brodwin, M., et al. 2013, *ApJ*, 768, 1
McDonald, M., Stalder, B., Bayliss, M., et al. 2016, *ApJ*, 817, 86
Mei, S., et al. 2009, *ApJ*, 690, 42
Moore, B. et al. 1999, *MNRAS*, 304, 465
Murray, S. S., Kenter, A., Forman, W. R., et al. 2005, *ApJS*, 161, 1
Noble, A. G., McDonald, M., Muzzin, A., et al. 2017, *ApJ*, 842, 21
Ocvirk, P., Pichon, C., & Teyssier, R. 2008, *MNRAS*, 390, 1326
Ostriker, J. P. & Tremaine, S. D., 1975, *ApJ*, 202, 113
Oteo, I., Ivison, R. J. et al. 2018, *ApJ*, 856, 72
Overzier, R. A. *A&ARv*, 24, 140
Papadopoulos, P. P., et al., 2000, *ApJ*, 528, 626
Peng, Y-j et al., 2010, *ApJ*, 721, 193
Planck Collaboration early results XXI, 2011a, *A&A*, 536, A21
Planck Collaboration early results XXV, 2011b, *A&A*, 536, A25
Planck Collaboration results XIII, 2016, *A&A*, 594, 13
Pozzi, F., Vignali, C. et al. 2012, *MNRAS*, 423 1909
Raichoor, A. & Andreon, S., 2012, *A&A*, 537A, 88
Riess, A. G., Macri, L. M., Hoffmann, S. L., et al. 2016, *ApJ*, 826, 56
Riess, A. G., Casertano, S. et al. 2018, *ApJ*, 855, 136
Roediger, J. C. & Courteau, S., 2015, *MNRAS*, 452, 3209
Rudnick, G., Hodge, J., Walter, F. et al. 2017, *ApJ*, 849, 27
Salomé, P., Combes, F., Edge, A. C. et al. 2006, *A&A*, 454, 437
Salomé, P., Combes, F., Revaz, Y. et al. 2008, *A&A*, 484, 317
Salomé, P., Combes, F., Revaz, Y. et al. 2011, *A&A*, 531, 85
Schmidt, M., 1959, *ApJ*, 129, 243
Scoville, N., Lee, N., Vanden Bout, P., et al. 2017, 837, 150
Sheth, R. K., & Diaferio, A., 2001, *MNRAS*, 322, 901
Smith, G. P., et al. 2010, *A&A*, 518, 1
Solomon, P. M., et al. 1997, *ApJ*, 478, 144
Solomon, P. M. & Vanden Bout, P. A., 2005, *ARA&A*, 43, 677
Speagle, J. S., Steinhardt, C. L. et al. 2014, *ApJS*, 214, 15
Stach, S. M., Swinbank, A. M., Smail, I. et al. 2017, *ApJ*, 849, 154
Stern, D., Eisenhardt, P., Gorjian, V., et al. 2005, *ApJ*, 631, 163
Tacconi, L. J., Genzel, R., Saintonge, A., et al. 2018, *ApJ*, 853, 179
Ueda, J., Iono, D. et al. 2012, *ApJ*, 745, 65
van der Wel, A., Franx, M. et al. 2014, *ApJ*, 788, 28
Vollmer, B., Wong, O. I., Braine, J., et al. 2012, *A&A*, 543, 33
Wagg, J., Pope, A., Alberts, S. et al. 2012, *ApJ*, 752, 91
Wagner, C. R., Brodwin, M., Snyder, G. F. et al. 2015, *ApJ*, 800, 107
Walter, F., Decarli, R. et al. 2016, *ApJ*, 833, 67
Wang, T. et al. 2016, *ApJ*, 828, 56
Webb, T. M. A. et al. 2013, *AJ*, 146, 84
Webb, T. M. A., Lowenthal, J., Yun, M. et al. 2017, *ApJ*, 844, 17
Whitmore, B. C., Brogan, C., Chandar, R. et al. 2014, *ApJ*, 795, 156
Whitaker, K. E., van Dokkum, P. G. et al. 2012, *ApJL*, 754, 29
Wright, A. H., Robotham, A. S. G. et al. 2017, *MNRAS*, 470, 283
Zeimann, G et al. 2013, *ApJ*, 779, 137

FIGURES

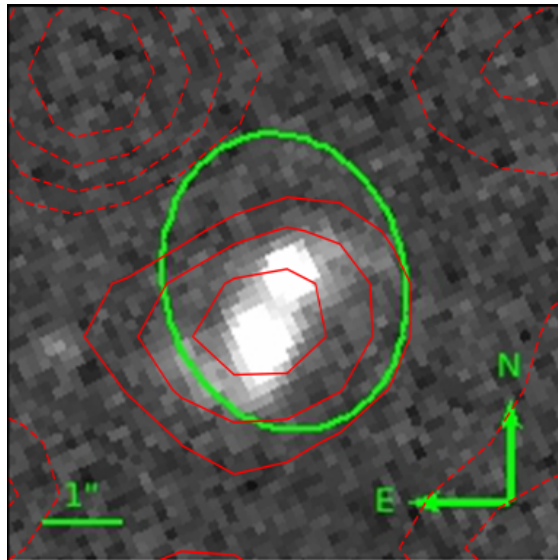
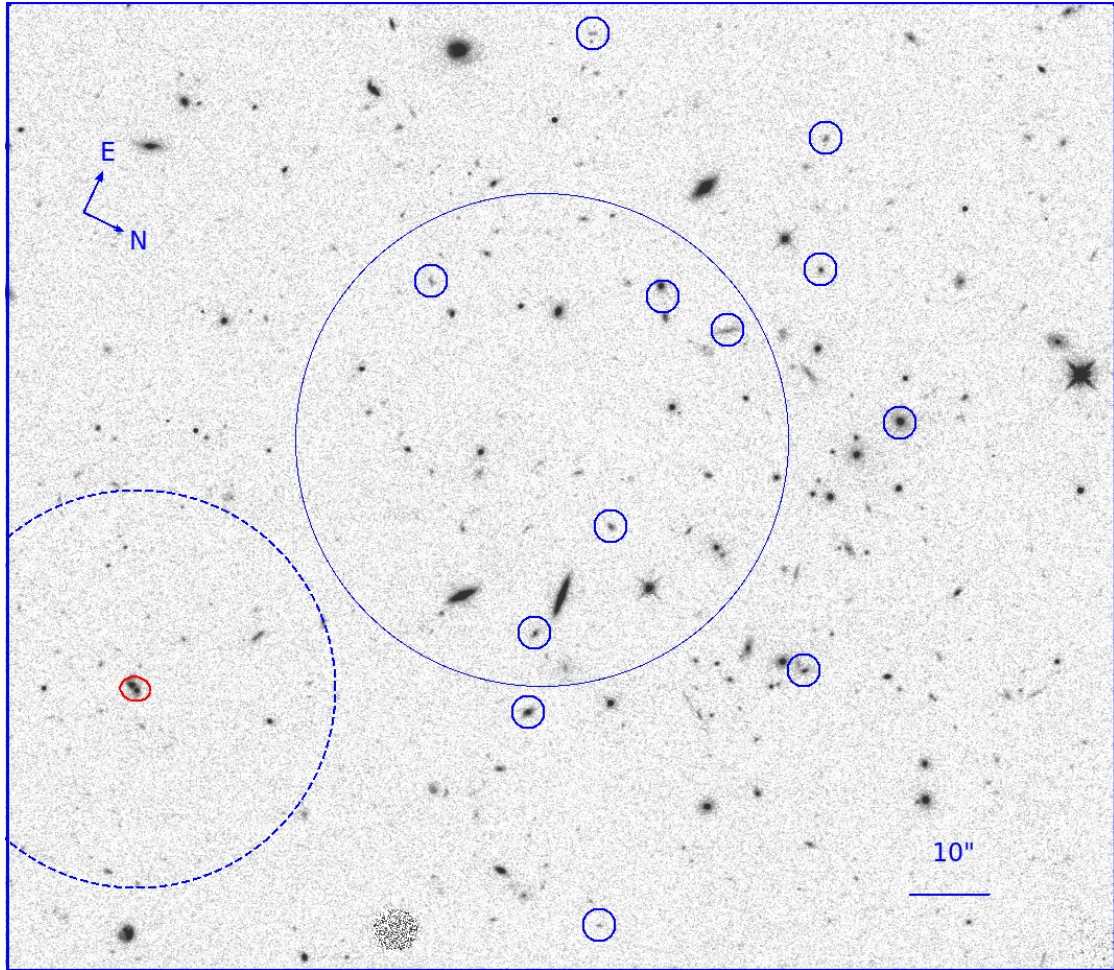


Fig. 1: Top: archival HST WFC3 image (width = $136''$; height = $119''$) of the cluster ISCS J1426.5+3339, taken with the F160W filter. The central, big, blue, and solid circle has a radius of 250 kpc. The NOEMA beam size with our two targets (red ellipse at the bottom left) and the NOEMA field of view (dashed blue arc) are shown. The small blue circles denote additional spectroscopically confirmed cluster members (Eisenhardt et al. 2008; Zeimann et al. 2013). Bottom: $7'' \times 7''$ zoom image showing the galaxy J142626.1+333827 and its southern companion J142626.1+333826. The green ellipse shows the NOEMA beam size (major axis = $3.69''$; minor axis = $2.98''$). Red contour levels correspond to the CO(2-1) detection, as in Fig. 2, left panel.

FIGURES

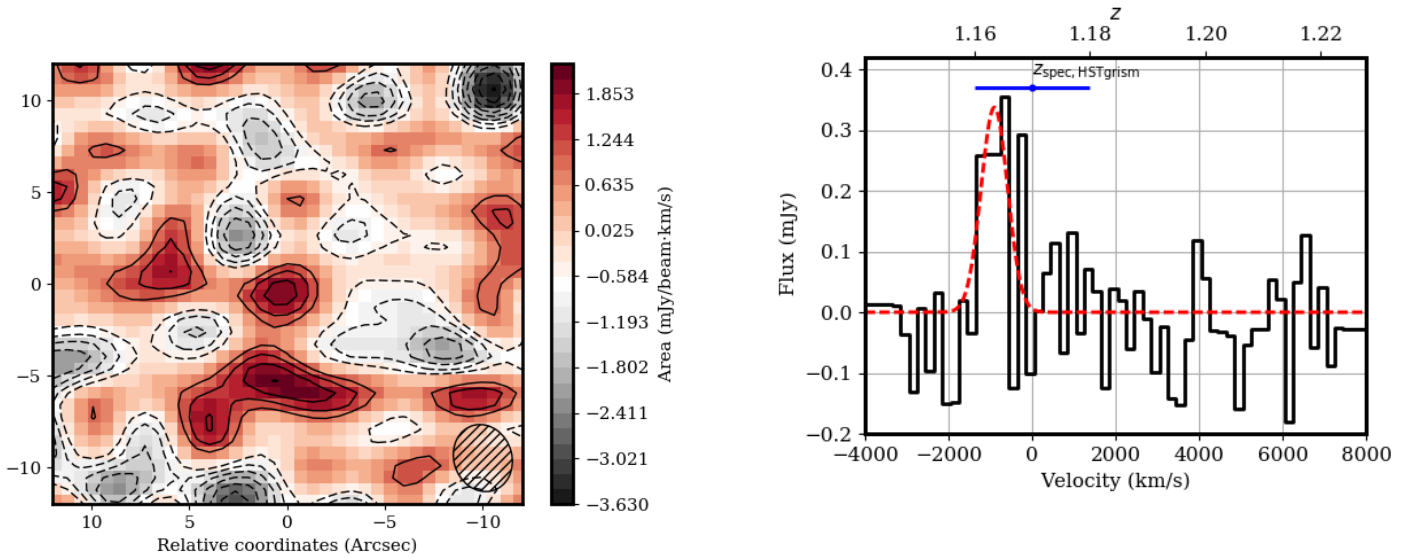


Fig. 2: Left: intensity map, cleaned and corrected for the NOEMA primary beam showing the detection of the two unresolved target sources at the center. Coordinates are reported as angular separations from the source J142626.1+333827. The velocity range considered is within -2,000 km/s and 0 km/s, corresponding to the CO(2-1) line, see right panel. Solid and dashed contour levels are superimposed and correspond to positive and negative fluxes, respectively. The dashed ellipse (bottom right) shows the beam size. Right: spectrum (black solid line) obtained with NOEMA within an aperture corresponding to the beam size at the location of the detection, i.e., the center of the intensity map. A resolution of 200 km/s is adopted. The best fit, baseline subtracted, is reported (red dashed line). The center and the length of the blue horizontal segment at the top of the spectrum correspond to the HST WFC3 spectroscopic redshift and its uncertainty, respectively (Zeimann et al. 2013).

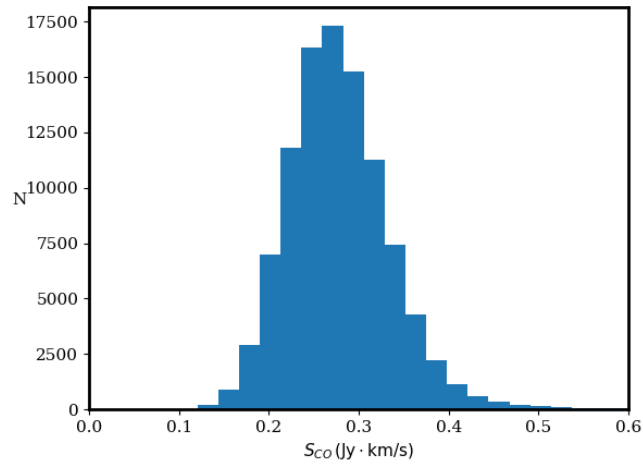


Fig. 3: Distribution of the integrated CO(2-1) fluxes, as derived from our Monte Carlo simulations.

FIGURES

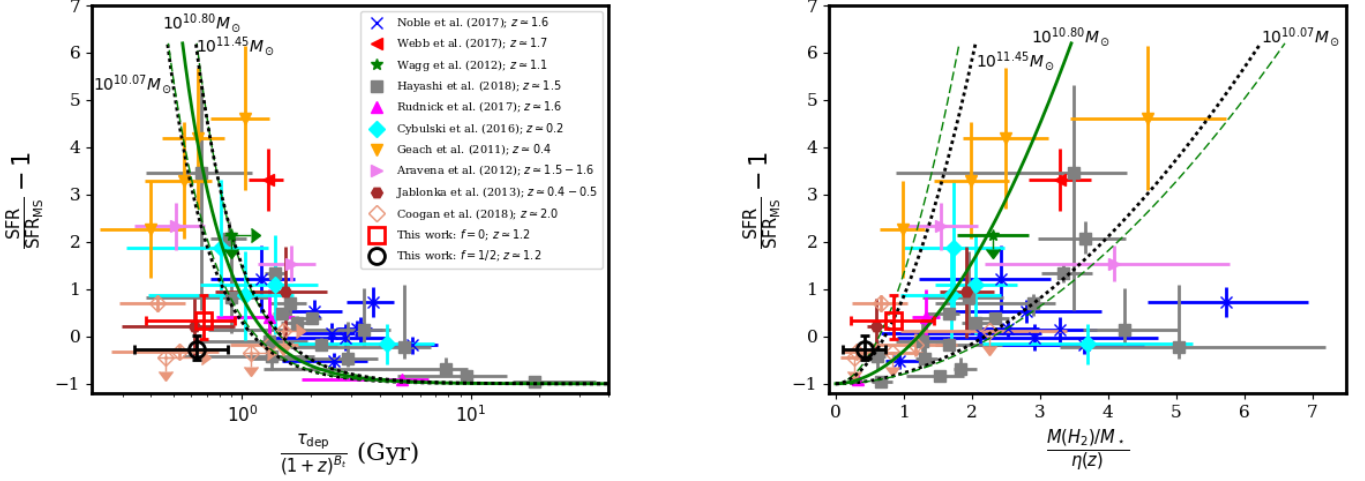


Fig. 4: Fractional offset from the star forming MS as a function of the molecular gas depletion timescale (left) and molecular gas to stellar mass ratio (right). Cluster galaxies at $0.2 \lesssim z \lesssim 2.0$ detected at CO are shown. Data points from this work refer to the cases where i) the two blended target sources equally contribute to the observed CO(2-1) flux ($f = 1/2$) or ii) only one of the two contributes to the observed flux ($f = 0$). In both panels the solid green curve is the scaling relation for field galaxies found by Tacconi et al. (2018) for galaxies with $\text{Log}(M_*/M_\odot)=10.8$ and with an effective radius equal to the mean value found by van der Wel et al. (2014) for star forming galaxies for given z and M_* . The green dashed lines show the statistical $1\text{-}\sigma$ uncertainties in the model. The dotted black lines show the same scaling relation as the solid green lines, but for different stellar masses $\text{Log}(M/M_*) = 10.07$ and 11.45 , that correspond to the stellar mass range spanned by the data points.

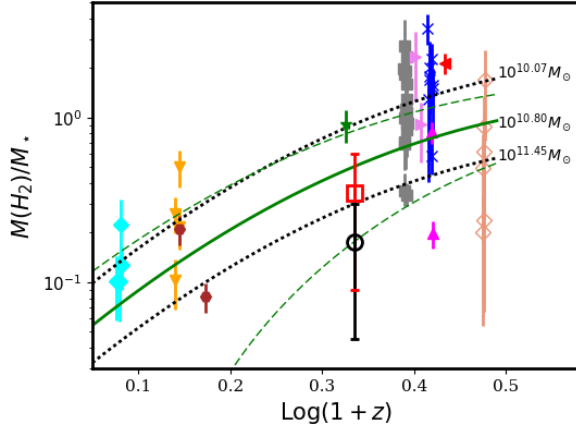


Fig. 5: Evolution of the molecular gas to stellar mass ratio as a function of the redshift for cluster galaxies at $0.2 \lesssim z \lesssim 2.0$ detected at CO. Color code is analogous to that of Fig. 4. The solid green curve is the scaling relation found by Tacconi et al. (2018) for field galaxies in the main sequence and with $\text{Log}(M_*/M_\odot)=10.8$, where an effective radius equal to the mean value found by van der Wel et al. (2014) for star forming galaxies for given z and M_* is assumed. The green dashed lines show the statistical $1\text{-}\sigma$ uncertainties in the model. The dotted black lines show the same scaling relation as the solid green line, but for different stellar masses $\text{Log}(M/M_*) = 10.07$ and 11.45 , that correspond to the stellar mass range spanned by the data points.

FIGURES

cluster ID	galaxy ID	z_{spec}	$\text{Log}(M_{\star}/M_{\odot})$	Flux ($\text{H}\alpha + [\text{NII}]$) ($10^{-17} \frac{\text{erg}}{\text{s cm}^2}$)	SFR($\text{H}\alpha$) (M_{\odot}/yr)	sSFR($\text{H}\alpha$) (Gyr^{-1})	$\tau_{\text{dep}}(\text{H}\alpha)$ (10^8 yr)	R_e (kpc)
(1)	(2)	(3)	(4)	(5)	(6)	(7)	(8)	(9)
ISCSJ1426.5+3339	J142626.1+333827	1.17±0.01	10.8 ± 0.5	79.1±5.3	127 ⁺¹⁰⁰ ₋₇₅	2.0 ^{+2.1} _{-1.9}	0.87 ^{+0.55} _{-0.70}	3.0
	J142626.1+333826	1.17±0.01	10.8 ± 0.5	83.7±4.8	134 ⁺¹⁰⁰ ₋₇₅	2.1 ^{+2.2} _{-2.0}	0.82 ^{+0.49} _{-0.63}	3.9

Table 1: Properties of the targets. (1) cluster and (2) galaxy name; (3) spectroscopic (HST WFC3) redshift of the galaxy; (4) galaxy stellar mass; (5) $\text{H}\alpha + [\text{NII}]$ line flux; (6) SFR($\text{H}\alpha$) estimated following Zeimann et al. (2013); (7) $\text{sSFR}(\text{H}\alpha) = \text{SFR}(\text{H}\alpha)/M_{\star}$; (8) $\tau_{\text{dep}}(\text{H}\alpha) = M(\text{H}_2)/\text{SFR}(\text{H}\alpha)$ estimated assuming that the two sources equally contribute to the observed CO(2-1) flux, i.e., $f = 1/2$; (9) effective radius estimated using SExtractor and the HST WFC3 image. Columns (3-5) are from Zeimann et al. (2013).

(1)	galaxy ID	J142626.1+333827 / J142626.1+333826
(2)*	z	1.163 ± 0.001, from CO(2-1)
(3)*	FWHM	(733 ± 200) km/s, from CO(2-1)
(4)*	$S_{\text{CO}(2-1)}$	(0.27 ^{+0.06} _{-0.05}) Jy km/s
(5)*	$L_{\text{CO}(2-1)}$	(4.9 ^{+1.1} _{-0.9}) × 10 ⁹ pc ² K km s ⁻¹
(6)*	$M(\text{H}_2)$	(2.2 ^{+0.5} _{-0.4}) × 10 ¹⁰ M_{\odot}
(7)*	continuum	< 33 μJy
(8)*	M_{dust}	< 4.2 × 10 ⁸ M_{\odot}
(9)	SFR(24 μm)	(52 ⁺²¹ ₋₁₅) M_{\odot}/yr ($f = 0$); (28 ⁺¹² ₋₈) M_{\odot}/yr ($f = 1/2$)
(10)	sSFR(24 μm)	(0.82 ^{+0.65} _{-0.64}) Gyr^{-1} ($f = 0$); (0.44 ^{+0.36} _{-0.34}) Gyr^{-1} ($f = 1/2$)
(11)	τ_{dep}	(4.2 ^{+1.6} _{-1.9}) × 10 ⁸ yr ($f = 0$); (3.9 ^{+1.4} _{-1.8}) × 10 ⁸ yr ($f = 1/2$)
(12)	$M(\text{H}_2)/M_{\star}$	0.35 ^{+0.25} _{-0.26} ($f = 0$); 0.17 ± 0.13 ($f = 1/2$)

Table 2: Summary of the results. Quantities marked with an asterisk (2-8) are estimated for the two blended sources. Quantities (9-12) refer to each of the two sources, separately. The two scenarios where both sources contribute equally to the observed CO(2-1) flux ($f = 1/2$) or only one of the two does ($f = 0$) are considered.